Mesoporous Co$_3$O$_4$ nanoneedle arrays for high-performance gas sensor

Zhen Wen, Liping Zhu *, Yaguang Li, Ziyue Zhang, Zhizhen Ye

State Key Laboratory of Silicon Materials, Department of Materials Science and Engineering, Cyrus Tang Center for Sensor Materials and Applications, Zhejiang University, Hangzhou 310027, PR China

ARTICLE INFO

ABSTRACT

Co$_3$O$_4$ nanoneedle arrays were successfully fabricated via a facile two-step approach, including the formation of needle-shaped Co(CO$_3$)$_{0.5}$(OH)·0.11H$_2$O followed by thermal conversion to mesoporous Co$_3$O$_4$. The Co$_3$O$_4$ nanoneedle arrays exhibit mesoporosity and quasi-single-crystalline structure, and can directly serve as gas sensors without the conventional film formation process, owing to the directly growth on the substrates and good ohmic contact with the electrodes. The Co$_3$O$_4$ nanoneedle arrays-based gas sensor showed high performance in ethanol detection. The highest sensitivity reached ∼89.6 for 100 ppm ethanol vapor and the optimal working temperature was as low as 130 °C. The high performance attributes to the unique structure of nanoneedle arrays with a variety of favorable features. More attractively, we find the special exposed crystal planes of Co$_3$O$_4$ affect the gas-sensing properties significantly.

1. Introduction

Cobalt oxide (Co$_3$O$_4$) nanomaterials are widely used in s heterogeneous catalysis, lithium-ion batteries, supercapacitors, optical and magnetic materials, and chemical sensors, where their performances are strongly dependent on their size and morphology [1–4]. The morphological control, including size, shape, surface structure, crystal orientation, stacking manners, aspect ratios and even crystalline densities, of nanomaterials is of essential importance [5,6]. Therefore, a large number of efforts have been focused on the controlled synthesis of nanostructured Co$_3$O$_4$ and many methods have been developed to synthesize nanomaterials with different morphologies and architectures, such as nanorods, nanowires, nanotubes, nanofibers, nanocubes, and nanoplatelets [7–9]. Among them, one-dimensional Co$_3$O$_4$ nanoarrays have been demonstrated to be an optimized architecture for boosting performance. Very recently, Wu's group reported the high capacity and rate capability of mesoporous Co$_3$O$_4$ nanowire arrays as anodes in lithium-ion batteries [10]. Wang *et al.* synthesized a freestanding Co$_3$O$_4$ nanowire arrays with enhanced electrochemical catalysis for detection of H$_2$O$_2$ [11]. Hui *et al.* supplied a crystalline Co$_3$O$_4$ nanowire arrays with good catalytic activity for the ozone catalytic oxidation of toluene [12]. Xia *et al.* prepared single-crystalline Co$_3$O$_4$ nanowire arrays for high performance supercapacitors [13].

Our group reported the novel rhombus-shaped Co$_3$O$_4$ nanorod arrays for gas sensors with high ethanol detection performance [14]. Nevertheless, few works dealt with Co$_3$O$_4$ nanoarray based gas sensors.

According to the sensing mechanisms of gas sensors, the adsorption/desorption processes mainly take place on the surface of the sensing layer and determine the response of the sensors [15,16]. Since the sensitivity of gas sensors is directly linked to the size, shape, exposed surface area of the sensing material, one-dimensional nanoarray structures possessing very high surface to volume ratios are attractive candidates for designing the next generation of sensors. Nanoarrays are of particular interest because of not only high surface-to-volume ratio and great miniaturization potential, but also high reaction rate [17]. The advantages of nanoarrays make their electrical properties extremely sensitive to surface-adsorbed species, which leads to a higher sensing performance [4,10,18]. Firstly, the large surface-to-volume ratio and nanoscale dimension facilitate gases diffusing into and from the nanostructure. Secondly, a lower detection limit is achieved because of a larger change in their electrical properties upon surface adsorption. Thirdly, the open space of the nanoarrays allows for easy contact and diffusion of the gas molecules into the inner region. Thus, exploring the gas sensing performance arising from the nanostructure arrays is demanding. According to statistics available, very few reports involve this research.

In this work, we present the fabrication of the needle-shaped Co$_3$O$_4$ arrays-based gas sensor. A rational and facile hydrothermal route is introduced, involving the formation of needle-shaped

* Corresponding author. Tel.: +86 571 87953139; fax: +86 571 87952625.
E-mail address: zlp1@zju.edu.cn (L. Zhu).

$Co(CO_3)_{0.5}(OH)\cdot0.11H_2O$ as the precursor and then thermal conversion to mesoporous Co_3O_4. The structure and morphology characterizations of the nanoneedle arrays were investigated by X-ray diffraction (XRD), Fourier transform infrared spectroscopy (FTIR), scanning electron microscopy (SEM), high-resolution transmission electron microscopy (HRTEM), thermo-gravimetric analysis (TGA), Raman spectrometer and N_2 sorption, respectively. The Co_3O_4 nanoneedle arrays can directly grow on the substrates and show robust mechanical adhesion to the supporting substrates, supplying a simple method to prepare a nanoarray-based gas sensor. The Co_3O_4 nanoneedles exhibit mesoporosity and quasi-single-crystalline structure. The Co_3O_4 nanoneedle arrays based gas sensor shows high-performance sensing properties in ethanol detection, owing to the unique structure of nanoneedle arrays with a variety of favorable features.

2. Experimental

2.1. Synthesis

All chemicals or materials were of analytical grade and used directly without any further purification prior to usage. In a typical synthesis, 5 mmol (1.45 g) of cobalt nitrate $(Co(NO_3)_2\cdot6H_2O)$, 10 mmol (0.37 g) of ammonium fluoride (NH_4F) and 10 mmol (1.50 g) of urea $(CO(NH_2)_2)$ were dissolved in 50 ml highly pure water (18.3 MΩ cm resistivity) under stirring at room temperature. After stirring for 10 min, the homogeneous solution was transferred into a 100 ml Teflon-lined stainless steel autoclave. Then, a piece of cleaned polycrystalline alumina ceramics plate (13.4 mm × 7 mm, 0.5 cm in thickness) which have been plated Ag–Pd finger regions (five pairs) as electrodes were immersed in the reaction solution against the inner wall of the autoclave and fixed by polyimide tapes. The autoclave was sealed and maintained at 95 °C for 24 h. After cooling down to room temperature, the substrate was removed, rinsed with distilled water several times, and dried at 60 °C under vacuum for 2 h. Finally, the as-prepared pink precursors were collected after annealing at 350 °C in air for 4 h.

2.2. Characterization

The crystal phase identification were investigated by XRD (Bede D1) system with Cu $K\alpha_1$ radiation ($\lambda = 0.15406$ nm). The morphologies of both the precursor and annealed products were investigated using SEM (Hitachi S-4800). Further structural analysis was carried out using HRTEM (FEI F20). TGA (SDT Q600) was carried out under air atmosphere at 10 °C min^{-1} in the temperature range 10–900 °C. Raman spectra were collected through a confocal microscopy Raman spectrometer (Jobin Yvon HR 800) at ambient conditions, using the radiation of 514 nm. FTIR (TENSOR 27) was characterized with DTGS detector by making pellets with KBr powder. Specific surface areas were computed from the results of N_2 physisorption at 77 K (TriStar II 3020) by using the Brunauer–Emmet–Teller (BET) and Barrett–Joyner–Halenda (BJH) The electrical characteristics were measured at room temperature in the dark using a semiconductor parameter analyzer (Agilent E5270B).

2.3. Gas-sensing measurements

The obtained sensors could be directly used for gas sensing measurements and were performed on an intelligent gas sensing analysis system (CGS-1TP, Beijing Elite Tech Co., Ltd., China). The analysis system offered an external temperature control (from room temperature to 500 °C), which could conductively adjust the sensor temperature with a precision of 1 °C. The sensors were laid on the temperature control and pre-heated at different operating temperatures for about 30 min. Two probes were pressed on sensor

electrodes by controlling the position adjustment in the analysis system. When the resistance of the sensor was stable, saturated target gas was injected into the test chamber (18 L in volume) by a micro-injector through a rubber plug. The saturated target gas was mixed with air (relative humidity was ~46%) by two fans. After the sensor resistance reached a new constant value, the test chamber was opened to recover the sensors in air. The sensor resistance and sensitivity were collected and analyzed by the system in real time. The photograph of the gas sensing analysis system is shown in Fig. 1(b). The gas response (S) is designated as the ratio R_g/R_a, where R_g is the sensor resistance of a mixture of target gas and air while R_a is in air. Response and recovery times are defined as the time needed for 90% of total resistance change on exposure to gas and air, respectively.

3. Results and discussion

The phase composition, morphology and structure of the precursor obtained by the hydrothermal method were firstly investigated systematically. Fig. 2(a) shows the XRD pattern of the precursor, which is indexed as $Co(CO_3)_{0.5}(OH)\cdot0.11H_2O$. All of the diffraction peaks are in good agreement with the standard Joint Committee on Powder Diffraction Standards (JCPDS) card No. 48-0083, which indicates that the precursor is a pure orthorhombic phase. From a typical SEM image of the precursor in Fig. 2(b), we can observe that large-scale and high density arrays are uniformly grown on the substrate. The inset shows that the products have average diameter of approximately 100 nm with needle-like tips, indicating they were characteristic of a one-dimensional growth along a specific direction. The cross-sectional SEM image shown in Fig. 2(c) indicates that the needle-shaped arrays with a length of about 5 μm are well aligned. An individual nanoneedle presented regular grass-blade-shaped morphology stemming from the bottom section and eventually developed into one inseparable part of a nanoneedle bundle. These nanoneedles among the bundle were originated from the same starting point and grew along the direction vertical to surface of the substrate. The TEM shown in Fig. 2(d) indicate that a single nanoneedle has a grass-blade-shaped morphology, with diameter in the range of 20–100 nm. The selected-area electron diffraction (SAED) pattern implies the precursor is single-crystalline in nature.

The thermo-decomposition behavior of the precursor was studied by thermal-gravimetric (TG) analysis. From the TG curve in Fig. 3(a), it is clear to find an apparent decomposition steps. The step shows an abrupt change of the curve with a weight loss of 26.4% at the temperature above 350 °C corresponding to the theoretical analysis of 25.6% and indicates the oxidation of the precursor. To better understand the possible phase changes, the precursor was annealed at 350 °C for 4 h and then analyzed by XRD, Raman and FTIR, respectively. The XRD pattern shown in Fig. 3(b) reveals that all of the peaks correspond well to cubic spinel Co_3O_4 phase (JCPDS card No.43-1003) and no diffraction peaks of $Co(CO_3)_{0.5}(OH)\cdot0.11H_2O$ are observed, which reveal the complete thermal conversion of the precursor to Co_3O_4. The Raman spectrum of the products measured at room temperature in Fig. 3(c) displays four bands located at 466, 508, 601, and 669 cm^{-1}, corresponding to the E_g, F_{2g}, F_{2g}, and A_{1g} modes of the spinel Co_3O_4 phase, respectively [1,19]. The Raman spectrum further demonstrates the as-synthesized product is pure cobalt oxide. Fig. 3(d) depicts the FTIR spectra of the products before and after annealing, respectively. The strong peaks at 3503 cm^{-1} are attributed to the molecular water and hydrogen-bond O–H groups [7]. The shoulder vibration at 3417 cm^{-1} can be assigned to the O–H groups interacting with fluoride or carbonate anions. The peaks centred at 1500, 829 and 743 cm^{-1} can be indexed to stretching vibration $\nu(OCO_2)$,
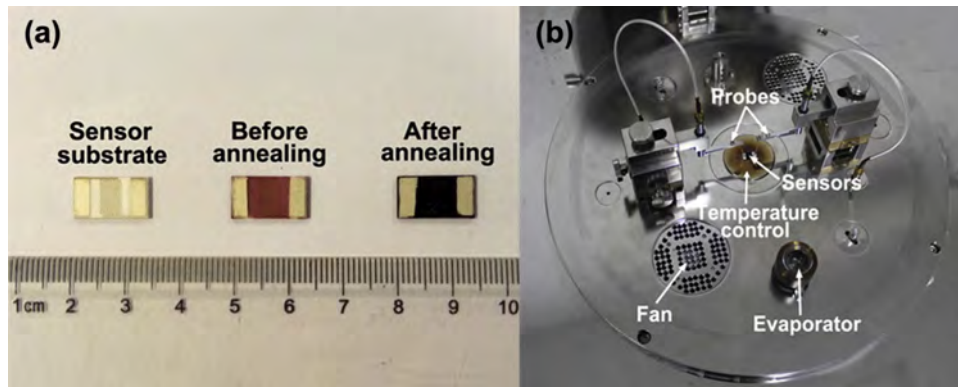
Fig. 1. (a) Top view of sensor substrate and sample sensors. (b) A photograph of the gas sensing analysis system.

$\delta(CO_3)$ and $\delta(OCO)$, respectively [20,21]. The presence of CO_3^{2-} is due to hydrolysis of urea and could be completely removed after calcination. The peaks at 964 and 522 cm^{-1} correspond to $\delta(Co-OH)$ and $\rho_w(Co-OH)$ bending modes [22]. Wide band at 3430 cm^{-1} indicates the presence of water in the samples. Two new distinct peaks at 574 and 665 cm^{-1} are related with the stretching vibrations of the metal oxygen bonds, which confirm the formation of the Co_3O_4 spinel oxide [7,13]. Thus, the FTIR spectroscopy results correspond well with the XRD and Raman results.

From the SEM image shown in Fig. 4(a), the needle-like morphology of Co_3O_4 is almost unaltered during the thermal conversion, which shows similar architecture to the precursor. Notably, from the inset high-magnification image, we observed that pores appeared on the surface. The typical TEM image in Fig. 4(b) shows an individual Co_3O_4 nanoneedle, with an average diameter of ~100 nm and a marked contrast compared to the precursor. The

HRTEM image in Fig. 4(c) taken from the area marked with a red square and the corresponding SAED pattern in Fig. 4(b) reveal the Co_3O_4 nanoneedle demonstrates highly oriented growth and quasi-single-crystalline nature [17]. The set of (1–11) planes with a crossing lattice spacing of 0.467 nm with the included angle of 70.5° indicate that the directly exposed crystal plane open to us is {10–1}. Thus, the Co_3O_4 nanoneedles mainly grow along the [1 0 1] direction and preferentially expose the {1 0 1} plane, which is simultaneously composed of Co^{3+} and Co^{2+} cations, rather than containing only Co^{2+} [23]. N_2 sorption was used for characterization of the porous structure of Co_3O_4 nanoneedles and gathering information about the specific surface area and pore size. The N_2 absorption–desorption isotherms at 77 K is shown in Fig. 4(d) with insets showing the pore size distribution. It can be observed that the isotherms are characteristic of a type IV with type H3 hysteresis loop which confirm the mesoporous structure [9]. BET
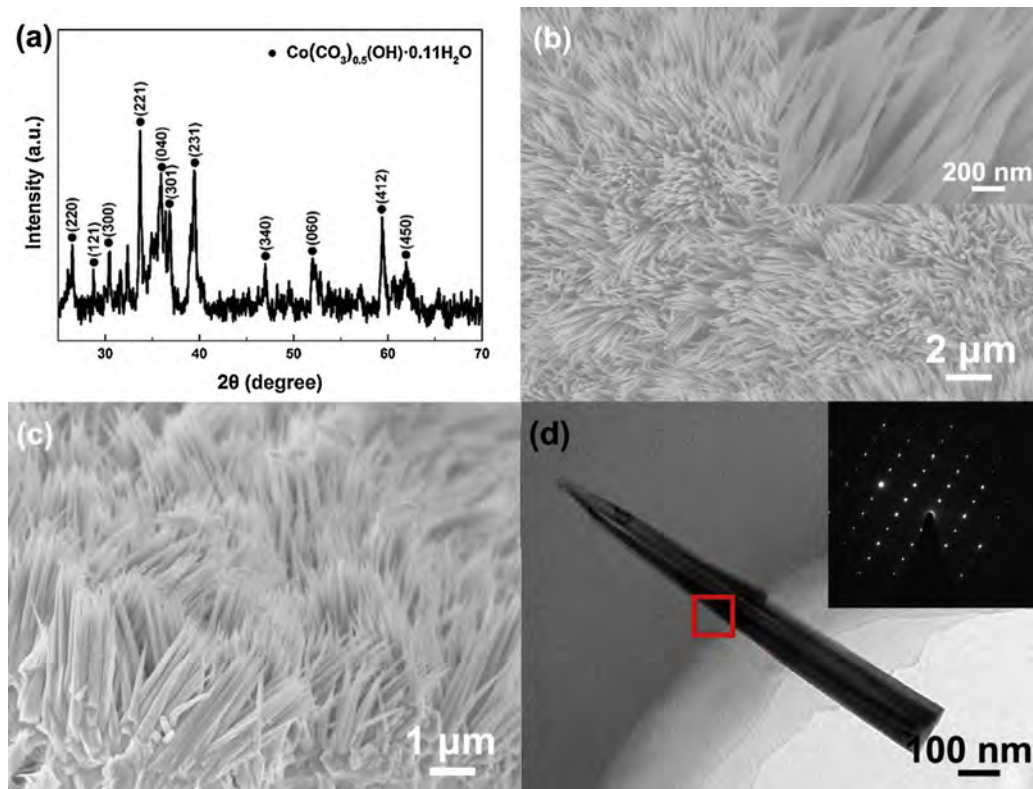

Fig. 2. Phase composition, morphological and structural characterization of the precursor $Co(CO_3)_{0.5}(OH)\cdot0.11H_2O$: (a) XRD pattern; (b) top view of SEM image; (c) cross-sectional SEM image; and (d) TEM image (inset shows the SAED pattern indicated by the red square).
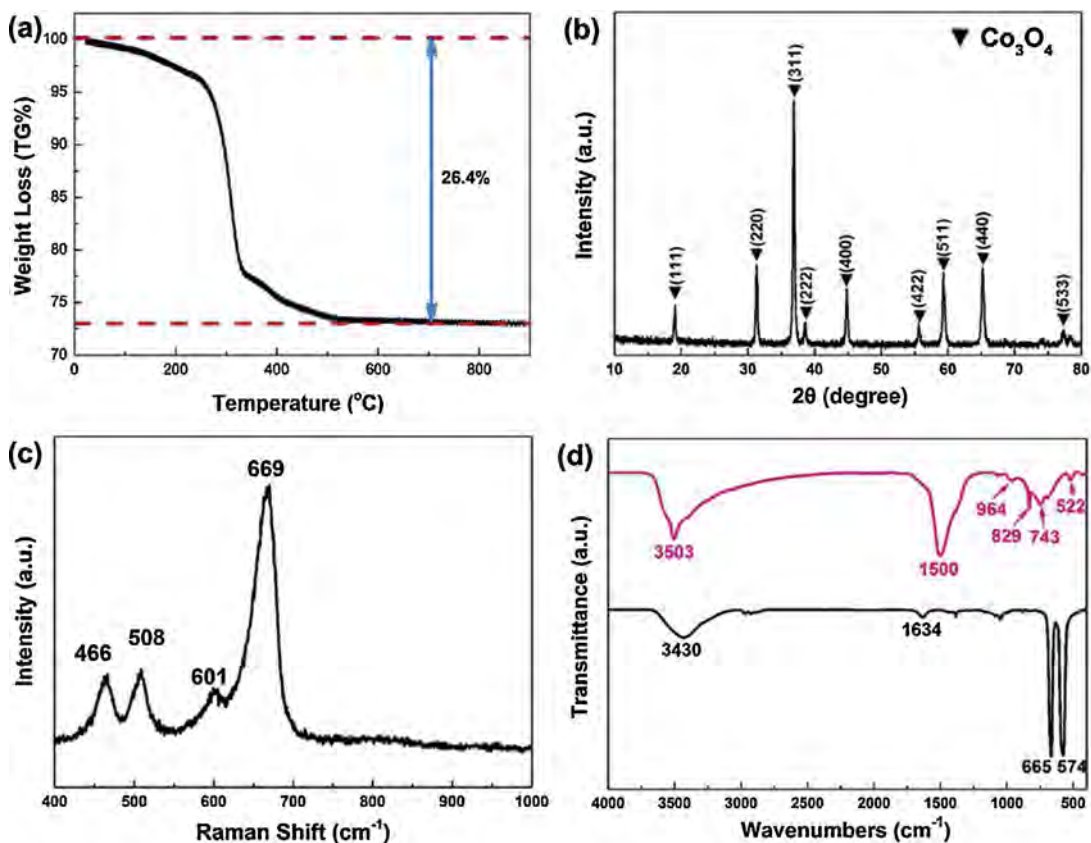
Fig. 3. (a) TG curve under air with a ramp of 10 °C min^{-1} of the precursor Co(CO$_3$)$_{0.5}$(OH)·0.11H$_2$O. (b) XRD patterns of the Co$_3$O$_4$ nanoneedle arrays. (c) Raman spectrum of the Co$_3$O$_4$ nanoneedle arrays. (d) FTIR spectra of the products before and after annealing at 350 °C.
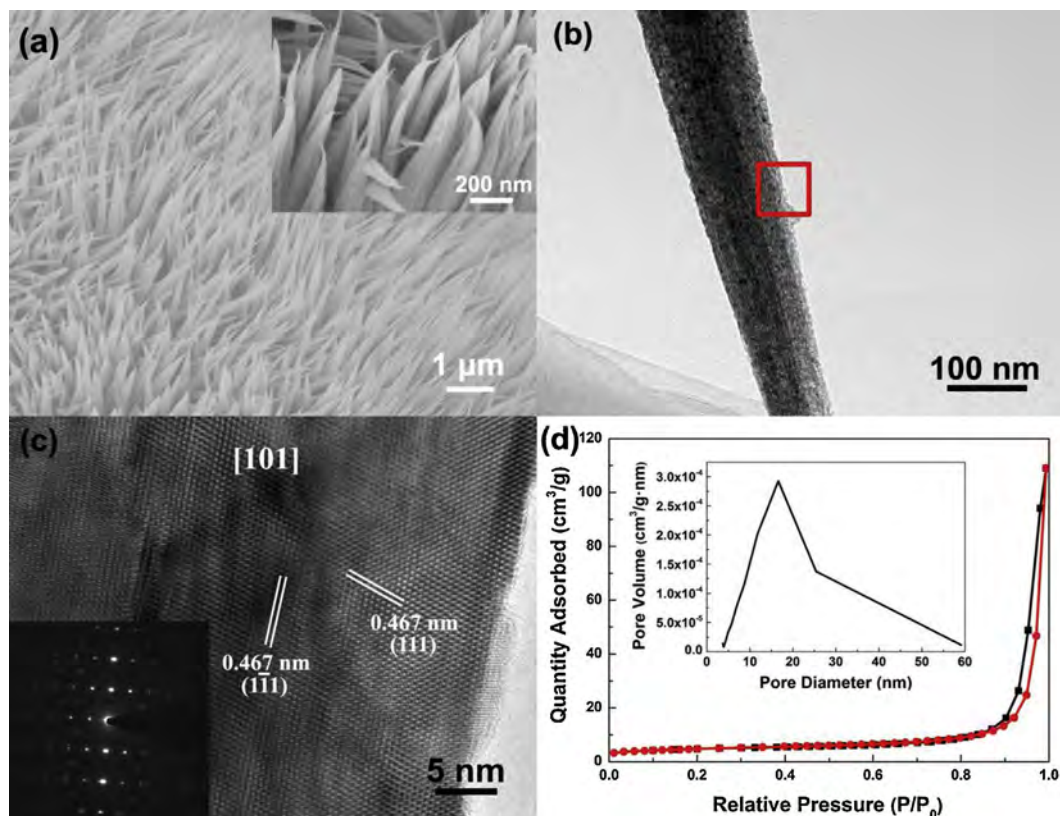

Fig. 4. (a) SEM image of Co$_3$O$_4$ nanoneedle arrays (high-magnification inset). (b) TEM image of an individual Co$_3$O$_4$ nanoneedle (inset shows the corresponding SAED pattern indicated by the red square). (d) N$_2$ adsorption/desorption isotherm curve of Co$_3$O$_4$ nanoneedle arrays and porous volume distribution of the pore size (inset).
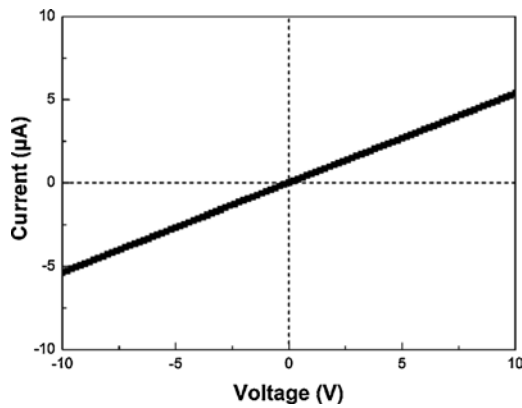
Fig. 5. I–V characteristics between the two neighboring electrodes, bridged by the Co$_3$O$_4$ nanoneedles, measured in air.

Fig. 7. The resistance change of the Co$_3$O$_4$ nanoneedle arrays gas sensor between 100 ppm concentration of ethanol and air at 130 °C.

measurement shows that the nanoneedle arrays have a surface area of 22.9 m^2/g. The pore size distribution (inset) shows a peak at 16.7 nm. In fact, the mesoporosity could be reasonably deduced from the pyrolysis and release of CO$_2$ and H$_2$O during the thermal conversion [17,24].

As a result of the large surface area and mesoporous structure revealed in the Co$_3$O$_4$ nanoneedle arrays, it is worthwhile to study their gas-sensing performance. Fig. 5 plots the current–voltage (I–V) characteristics between the two neighboring electrodes bridged by the Co$_3$O$_4$ nanoneedles in the air. The current increased linearly with applied bias. Such linear behavior reveals good ohmic contacts between the nanoneedles and the electrodes, which is very important for the electrical properties because this ensures that all upcoming sensing behaviors of sensors represent the properties of the nanoneedles but not the contact between the materials and the electrodes [15].

To conduct gas-sensing measurements, 100 ppm ethanol was introduced into a sealed chamber. The optimal working temperature for maximum response was determined and the results are shown in Fig. 6. The gas sensor attained the highest response at 130 °C, much lower than those reported for Co$_3$O$_4$ sensors [25,26]. The response was found to increase with the operating temperature, and then decrease with a further rise of the operating temperature. This behavior can be explained from the kinetics and dynamic of gas adsorption and desorption on the surface of Co$_3$O$_4$ or similar semiconducting metal oxides [27–29].

Fig. 7 shows the resistance changes between 100 ppm concentration of ethanol and air at 130 °C. As the ethanol is injected, the resistance of the sensor increases exponentially, and recovers to their initial state after exposing to air. The resistance undergoes
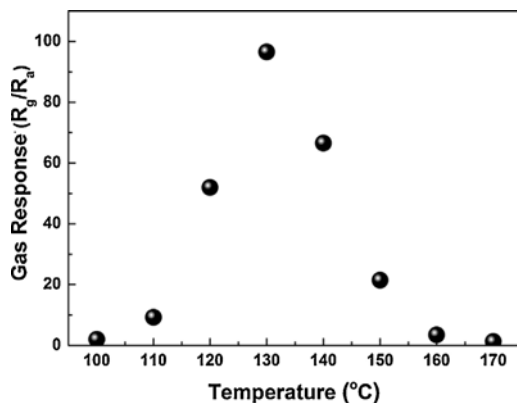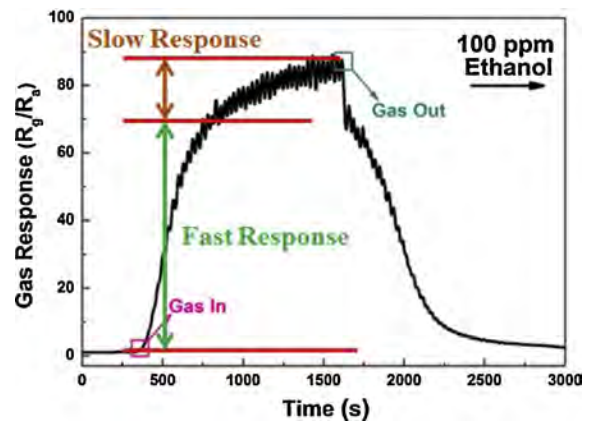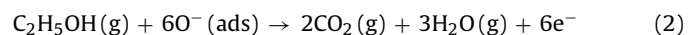
a drastic ascent on the injection of ethanol vapor and is mostly recovered to its initial value after the test gas is released, in agreement with that of a typical p-type semiconductor in the entire working temperature range. Notably, the curve can be broken into two parts: the "fast" (steep slope) and "slow" (shallow slope) response. We attribute this phenomenon to different energy binding sites with gas molecular of Co^{2+} and Co^{3+} [23]. Compared to our previous report [30], the sensitivity of needle-like Co$_3$O$_4$ arrays based gas sensor is much better than the rhombic ones can be attributed to different exposed crystal planes.

The gas sensing mechanism is usually believed to involve two steps. Primarily, the surface of Co$_3$O$_4$ is readily covered with the monolayer configuration of negatively charged chemisorbed oxygen (Eq. (1)) [8,31]. At the sensing temperature, the adsorption of negatively charged oxygen can generate the holes for conduction, which leads to the formation of a charge accumulation layer on the surface and the reaction kinetics is described as follows: $(1) \frac{1}{2}O_2(g) \rightarrow O^-(ads) + h^\bullet$

Therefore, when the ethanol is introduced into the test chamber, the charged carrier accumulation layer near the surface is thinned by the electrochemical interaction between O$^-$ (ads) and C$_2$H$_5$OH molecules (Eq. (2)), which releases free electrons and neutralizes the holes in the Co$_3$O$_4$ (Eq. (3)) and increases the resistances of the Co$_3$O$_4$ nanoneedles until a dynamic equilibrium condition is obtained [8,30]. The following gas-sensing reactions can be considered under the assumption of full oxidation of C$_2$H$_5$OH by O$^-$ (ads):

$$C_2H_5OH(g) + 6O^-(ads) \rightarrow 2CO_2(g) + 3H_2O(g) + 6e^- \qquad (2)$$

$$e^- + h^\bullet \rightarrow Null \qquad (3)$$

Hereafter, when the ethanol flow stopped, oxygen molecules in the air are adsorbed on the surface of the Co$_3$O$_4$ nanoneedles, and resistance of the sensor decreased to their initial values.

Fig. 8 shows the representative response and recovery curve of the Co$_3$O$_4$ nanoneedle array gas sensor to ethanol with concentrations ranging from 10 to 1000 ppm at 130 °C. The response increases rapidly with the concentration of ethanol in the range of 10–200 ppm. Above 200 ppm, the increase of response turns slow with the ethanol concentration rising. Finally, the sensitivity reaches saturation at above 500 ppm. The curve shows that the sensor could detect ethanol gas in a wide range of concentrations, starting with the minimum concentration of 10 ppm. Moreover, the inset shows the nearly linear calibration curve in the range of 10–100 ppm, which confirms that the sensor is quantitatively for low concentration ethanol gas detection.
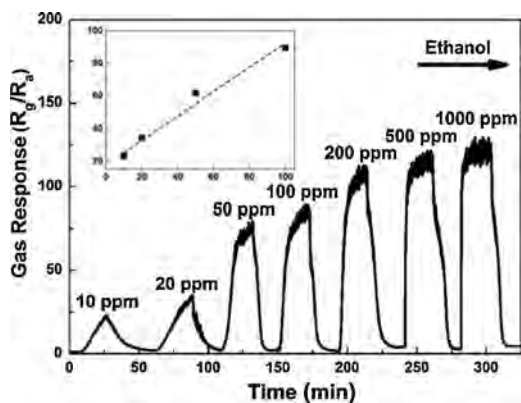

Fig. 6. Gas response of the Co$_3$O$_4$ nanoneedle arrays gas sensor as a function of different working temperatures to 100 ppm ethanol.

Fig. 8. The representative response and recovery curve of the Co_3O_4 nanoneedle arrays gas sensor to ethanol with concentrations ranging from 10 to 1000 ppm at 130 °C (inset shows the linear dependence of the gas response in the range of 10–100 ppm).

Fig. 10. Gas response to 100 ppm ethanol (RH ~46%) repeated with 30 times test during three months.

The selectivity of the Co_3O_4 nanoneedle array gas sensor to several reducing gases at 130 °C is tested and the results are shown in Fig. 9. The response to 100 ppm ethanol vapor is 89.6, which is significantly higher than all the other gases under the same concentration. The sensor shows a low response to acetone, methanol, carbon monoxide and hydrogen. The high anti-interference ability ascribes to the different binding energies for adsorption and desorption with O^- on the surface of Co_3O_4 at a low temperature. When the operating temperature reaches 130 °C, the sensor possesses the good selectivity to ethanol. The high response coupled with high sensing behavior makes it a good candidate for fabricating ethanol sensors.

Finally, the response of the sensor to 100 ppm ethanol is repeatedly tested for a period of 3 months with 30 times test as shown in Fig. 10. The mean response and standard error are calculated to be 89.6 and 10.5, showing a relative error of ~11.7%. Therefore, we can conclude that the stability of this material is good enough in long time detection of ethanol.

We believe that the high-performance for ethanol detection can be attributed to the unique structures of Co_3O_4 nanoneedle arrays with a variety of favorable features. Firstly, the as-prepared nanoneedle arrays can still stick to the substrate firmly even after strong ultrasonication over 30 min, suggesting the robust adhesion between the materials and the supporting substrates. After annealing, such contacts would be much stronger because of the improved crystallinity, which also dramatically increases the long-term stability of the devices. Good ohmic contact with the electrodes and
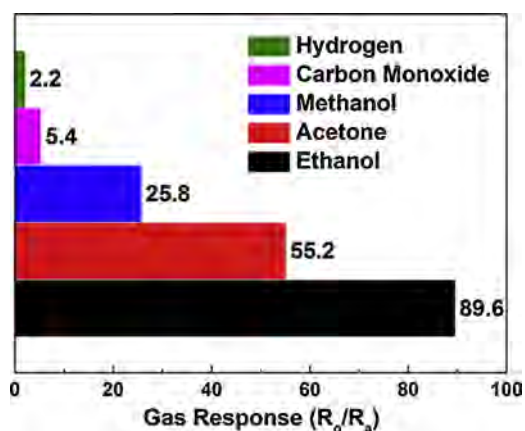
intensive contact with the substrates make it possible to use Co_3O_4 nanoneedle arrays directly as gas sensors without the conventional film formation process [15,32]. Secondly, the nanoneedle arrays are randomly oriented, which provides electrical paths between the neighboring electrodes. The open space between individual nanoneedle allows for easy contact and diffusion of the gas molecular into the inner region and facilitates every nanoneedle to participate in the gas sensing reaction. The nanoarrays also offer a short diffusion length for carriers and a long pathway for gas molecular absorption [33,34]. Thirdly, the special exposed crystal planes of Co_3O_4 affect the gas-sensing properties significantly. We consider the rapid response arises from the reaction between the gas molecular and the O^- adsorbed on the low-energy binding sites of Co^{3+}, and the slow response arises from the reaction at the higher-energy binding sites of Co^{2+} [23]. So, this work will further open the new directions to synthesize the special exposed crystal planes of Co_3O_4. The last but not the least, numerous nanopores appeared on the surface of nanoneedle during the thermal treatment, which increases the specific surface area tremendously. The high surface-to-volume ratio can provide more active reaction sites for adsorption and transport of gas molecules. Moreover, the mesoporous structures allow the gas molecules to easily penetrate and adsorb on the surface, leading to fast response and recovery as well as high response [35,36].

4. Conclusions

We have successfully synthesized needle-shaped Co_3O_4 nanoarrays via a facile hydrothermal route involving the formation of needle-shaped $Co(CO_3)_{0.5}(OH)·0.11H_2O$ as the precursor followed by thermal conversion to mesoporous Co_3O_4. It is noted that the nanoneedle arrays exhibit mesoporosity and quasi-single-crystalline structure. Good ohmic contact with the electrodes and intensive contact with the substrates avoided complicated fabrication process of gas sensors. The nanoneedle arrays-based gas sensor showed high-performance in ethanol detection. The response to 100 ppm ethanol gas reached ~89.6 and the optimal working temperature was as low as 130 °C. Meanwhile, the sensor can detect ethanol at a low detection limit (<10 ppm). The high ethanol gas sensing performance of the Co_3O_4 nanoneedle arrays can be explained by a typical p-type conductive behavior with the one-dimension structure, mesoporosity, large specific surface area and the open space of nanoneedle arrays. Moreover, we find the special exposed crystal planes of Co_3O_4 affect the gas-sensing properties significantly. The results demonstrate that the Co_3O_4 nanoarrays are very promising for the fabrication of cost effective and high-performance gas sensors.

Fig. 9. Gas response of the Co_3O_4 nanoneedle arrays gas sensor with several reducing gases (100 ppm) at 130 °C.

Acknowledgements

References

[1] W.M. Mei, J. Huang, L.P. Zhu, Z.Z. Ye, Y. Mai, J.P. Tu, Synthesis of porous rhombus-shaped Co_3O_4 nanorod arrays grown directly on a nickel substrate with high electrochemical performance, J. Mater. Chem. 22 (2012) 9315–9321.

[2] C.Y. Ma, Z. Mu, J.J. Li, Y.G. Jin, J. Cheng, G.Q. Lu, et al., Mesoporous Co_3O_4 and Au/Co_3O_4 catalysts for low-temperature oxidation of trace ethylene, J. Am. Chem. Soc. 132 (2010) 2608–2613.

[3] S.K. Meher, G.R. Rao, Ultralayered Co_3O_4 for high-performance supercapacitor applications, J. Phys. Chem. C 115 (2011) 15646–15654.

[4] W.Y. Li, L.N. Xu, J. Chen, Co_3O_4 nanomaterials in lithium-ion batteries and gas sensors, Adv. Funct. Mater. 15 (2005) 851–857.

[5] C.C. Li, X.M. Yin, T.H. Wang, H.C. Zeng, Morphogenesis of highly uniform $CoCO_3$ submicrometer crystals and their conversion to mesoporous Co_3O_4 for gas-sensing applications, Chem. Mater. 21 (2009) 4984–4992.

[6] X. Xie, W. Shen, Morphology control of cobalt oxide nanocrystals for promoting their catalytic performance, Nanoscale 1 (2009) 50–60.

[7] Y. Liu, G. Zhu, B. Ge, H. Zhou, A. Yuan, X. Shen, Concave Co_3O_4 octahedral mesocrystal: polymer-mediated synthesis and sensing properties, Crystengcomm 14 (2012) 6264–6270.

[8] K.I. Choi, H.R. Kim, K.M. Kim, D. Liu, G. Cao, J.H. Lee, C_2H_5OH sensing characteristics of various Co_3O_4 nanostructures prepared by solvothermal reaction, Sens. Actuators B Chem. 146 (2010) 183–189.

[9] N. Yan, L. Hu, Y. Li, Y. Wang, H. Zhong, X. Hu, et al., Co_3O_4 nanocages for high-performance anode material in lithium-ion batteries, J. Phys. Chem. C 116 (2012) 7227–7235.

[10] Y. Li, B. Tan, Y. Wu, Mesoporous Co_3O_4 nanowire arrays for lithium ion batteries with high capacity and rate capability, Nano letters 8 (2007) 265–270.

[11] J. Xu, J. Cai, J. Wang, L. Zhang, Y. Fan, N. Zhang, et al., Facile synthesis of hierarchically porous Co_3O_4 nanowire arrays with enhanced electrochemical catalysis, Electrochem. Commun. 25 (2012) 119–123.

[12] K.N. Hui, C.L. Yin, K.S. Hui, J.Y. Lee, M. Li, S.K. Lee, et al., Synthesis of Co_3O_4 nanowire arrays supported on Ni foam for removal of volatile organic compounds, J. Nanosci. Nanotechnol. 12 (2012) 3563–3566.

[13] X.H. Xia, J.P. Tu, Y.Q. Zhang, Y.J. Mai, X.L. Wang, C.D. Gu, et al., Freestanding Co_3O_4 nanowire array for high performance supercapacitors, RSC Adv. 2 (2012) 1835–1841.

[14] Z. Wen, L.P. Zhu, W.M. Mei, Y.G. Li, L. Hu, L.W. Sun, et al., A facile fluorine-mediated hydrothermal route to controlled synthesis of rhombus-shaped Co_3O_4 nanorod arrays and their application in gas sensing, J. Mater. Chem. A 1 (2013) 7511–7518.

[15] H. Nguyen, S.A. El-Safty, Meso- and macroporous Co_3O_4 nanorods for effective VOC gas sensors, J. Phys. Chem. C 115 (2011) 8466–8474.

[16] A.K. Srivastava, Detection of volatile organic compounds (VOCs) using SnO_2 gas-sensor array and artificial neural network, Sens. Actuators B Chem. 96 (2003) 24–37.

[17] Y. Wang, H. Xia, L. Lu, J. Lin, Excellent performance in lithium-ion battery anodes: rational synthesis of $Co(CO_3)_{0.5}(OH)·0.11H_2O$ nanobelt array and its conversion into mesoporous and single-crystal Co_3O_4, ACS Nano 4 (2010) 1425–1432.

[18] X.Y. Xue, S. Yuan, L.L. Xing, Z.H. Chen, B. He, Y.J. Chen, Porous Co_3O_4 nanoneedle arrays growing directly on copper foils and their ultrafast charging/discharging as lithium-ion battery anodes, Chem. Commun. 47 (2011) 4718–4720.

[19] V.G. Hadjiev, M.N. Iliev, I.V. Vergilov, The Eaman spectra of Co_3O_4, J. Phys. C Solid State Phys. 21 (1988) L199.

[20] X. Xie, P. Shang, Z. Liu, Y. Lv, Y. Li, W. Shen, Synthesis of nanorod-shaped cobalt hydroxycarbonate and oxide with the mediation of ethylene glycol, J. Phys. Chem. C 114 (2010) 2116–2123.

[21] Z. Zhao, F. Geng, J. Bai, H.M. Cheng, Facile and controlled synthesis of 3D nanorods-based urchinlike and nanosheets-based flowerlike cobalt basic salt nanostructures, J. Phys. Chem. C 111 (2007) 3452–3848.

[22] R. Xu, H.C. Zeng, Dimensional control of cobalt-hydroxide-carbonate nanorods and their thermal conversion to one-dimensional arrays of Co_3O_4 nanoparticles, J. Phys. Chem. B 107 (2003) 12643–12649.

[23] X. Xie, Y. Li, Z.Q. Liu, M. Haruta, W. Shen, Low-temperature oxidation of CO catalysed by Co_3O_4 nanorods, Nature 458 (2009) 746–749.

[24] L.P. Zhu, Z. Wen, W.M. Mei, Y.G. Li, Z.Z. Ye, Porous CoO nanostructure arrays converted from rhombic $Co(OH)F$ and needle-like $Co(CO_3)_{0.5}(OH)·0.11H_2O$ and their electrochemical properties, J. Phys. Chem. C 117 (2013) 20465–20473.

[25] A.M. Cao, J.S. Hu, H.P. Liang, W.G. Song, L.J. Wan, X.L. He, et al., Hierarchically structured cobalt oxide ($Co3O4$): the morphology control and its potential in sensors, J. Phys. Chem. B 110 (2006) 15858–15863.

[26] J.W. Yoon, J.K. Choi, J.H. Lee, Design of a highly sensitive and selective C_2H_5OH sensor using p-type $Co3O4$ nanofibers, Sens. Actuators B Chem. 161 (2012) 570–577.

[27] M. Ghasdi, H. Alamdari, CO sensitive nanocrystalline $LaCoO_3$ perovskite sensor prepared by high energy ball milling, Sens. Actuators B Chem. 148 (2010) 478–485.

[28] J. Herrán, O. Fernández-González, I. Castro-Hurtado, T. Romero, G. G^{a} Mandayo, E. Castaño, Photoactivated solid-state gas sensor for carbon dioxide detection at room temperature, Sens. Actuators B Chem. 149 (2010) 368–372.

[29] N. Yamazoe, J. Fuchigami, M. Kishikawa, T. Seiyama, Interactions of tin oxide surface with O_2, H_2O and H_2, Surf. Sci. 86 (1979) 335–344.

[30] Z. Wen, L.P. Zhu, W.M. Mei, L. Hu, Y.G. Li, L.W. Sun, et al., Rhombus-shaped Co_3O_4 nanorod arrays for high-performance gas sensor, Sens. Actuators B Chem. 186 (2013) 172–179.

[31] S. Pokhrel, C.E. Simion, V. Quemener, N. Bârsan, U. Weimar, Investigations of conduction mechanism in Cr_2O_3 gas sensing thick films by ac impedance spectroscopy and work function changes measurements, Sens. Actuators B Chem. 133 (2008) 78–83.

[32] Z. Wen, L.P. Zhu, L. Li, L.W. Sun, H. Cai, Z.Z. Ye, A fluorine-mediated hydrothermal method to synthesize mesoporous rhombic ZnO nanorod arrays and their gas sensor application, Dalton Trans. 42 (2013) 15551–15554.

[33] J.X. Wang, X.W. Sun, Y. Yang, H. Huang, Y.C. Lee, O.K. Tan, et al., Hydrothermally grown oriented ZnO nanorod arrays for gas sensing applications, Nanotechnology 17 (2006) 4995–4998.

[34] J.J. Hassan, M.A. Mahdi, C.W. Chin, H. Abu-Hassan, Z. Hassan, A high-sensitivity room-temperature hydrogen gas sensor based on oblique and vertical ZnO nanorod arrays, Sens. Actuators B Chem. 176 (2013) 360–367.

[35] T. Wagner, S. Haffer, C. Weinberger, D. Klaus, M. Tiemann, Mesoporous materials as gas sensors, Chem. Soc. Rev. 42 (2013) 4036–4053.

[36] Y. Cui, Q. Wei, H. Park, C.M. Lieber, Nanowire nanosensors for highly sensitive and selective detection of biological and chemical species, Science 293 (2001) 1289–1292.

Biographies

Zhen Wen received his B.S. degree at China University of Mining and Technology in 2011. He is currently pursuing Ph.D. degree at Zhejiang University. His research interests are in the area of nanomaterials and their application in gas sensors.

Liping Zhu received her B.Sc. (1988) and M.Sc. (1991) degrees in materials science from Zhejiang University. She studied in Hiroshima University in Japan as a doctoral student from 1998 to 2002. Then she joined the Materials Department of Zhejiang University since 2002. Her current research interests include semiconductor materials, photo-electronic thin films, nanomaterials and their application in devices.

Yaguang Li received B.S. degree at Yanshan University in 2010. He is currently pursuing MS degree at Zhejiang University. His research interests are in the area of nanomaterials and their application in catalysis.

Ziyue Zhang received B.S. degree at Northwestern Polytechnical University in 2013. She is currently pursuing Ph.D. degree at Zhejiang University. Her current fields of interests include design and synthesis of nanomaterials and study their gas sensing properties.

Zhizhen Ye received his B.S. degree in electrical engineering, received his M.S. degree and his Ph.D. in optical engineering from Zhejiang University in 1981, 1984 and 1987, respectively. He has been a professor of materials science and engineering since 1994. His research interests are in the area of heterogrowth and devices fabrication of silicon-based thin films.